NUMERICAL STUDY AND COMPARISON OF

ELECTROMAGNETIC SCATTERING

FROM OCEAN SURFACES

By

BRENT H. DAVIS

Bachelor of Science
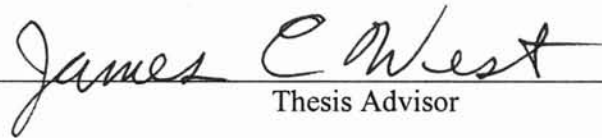
Oklahoma State University
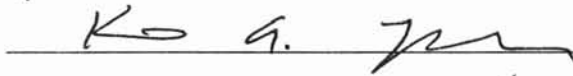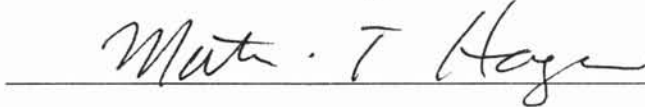
Stillwater, Oklahoma

2000

Submitted to the Faculty of the
Graduate College of the
Oklahoma State University
in partial fulfillment of
the requirements for
the Degree of
MASTER OF SCIENCE
May, 2002

NUMERICAL STUDY AND COMPARISON OF

ELECTROMAGNETIC SCATTERING

FROM OCEAN SURFACES

Thesis Approved:

James C West

Thesis Advisor

_K. G._

Mat. T. Hoge

Timothy D. Pett

Dean of the Graduate College

ACKNOWLEDGEMENTS

TABLE OF CONTENTS

LIST OF FIGURES

CHAPTER 1

INTRODUCTION

Since the discovery of radar, electromagnetic waves have been used for a variety

of tasks from communications to targeting to weather sensing to remote sensing of the

earth. Using the known properties of electromagnetic propagation has allowed people to

predict and model the reflections and backscattering caused by objects illuminated by the

radiated electromagnetic field. When radars are used on the sea, there is a great

challenge in predicting the reflections and backscattering because of the sea's constantly

changing surface. The changing ocean surface results in random backscatter known as

"sea clutter" that can mask the returns from targets of interest. When the illumination

grazing angle (relative to horizontal) is very small, clutter is characterized by very spiky

responses of the horizontally polarized (HH) incident/reflected signals. This clutter

sometimes results in what are known as "sea spikes," which are incidents when the HH

reflected signals exceed the vertically polarized (VV) reflected signals. Sea spikes are of

particular interest because they are not predicted at low grazing angles by standard rough

surface scattering models such as the two-scale model [9,12,13] or Kirchhoff

approximation [10,12] that assume the roughness is uniformly distributed across the

surface. Sea spikes have been observed to be much more common when the radar look

direction is upwind rather than when looking crosswind or downwind [13]. Because

there are so many variables that affect electromagnetic scattering from a sea surface,

there are still many aspects that are not well understood.

Studies have shown that sea spikes are associated with breaking or plunging waves, but the exact mechanism that creates these spikes is not yet fully understood [5,14,17]. Both plunging waves with whitecaps and spilling waves with steep faces have produced sea spikes. One such study associated whitecaps with approximately 30% of sea spikes while the rest were attributed to waves with very steep features [5].

There are several mechanisms that have been suggested as the origins of the sea spike behavior. Wedge diffraction [25,26], spray from the waves [27], and multipath scattering from the plume of spilling and breaking waves have all been suggested [15,17]. Currently, multipath scattering has received the most attention, and it has been studied both theoretically and experimentally. Trizna's studies helped develop Weibull distributions for scattering due to small-scale roughness and for sea spike scattering associated with deterministic waves [11].

Holiday et al's study [22] concluded that there was no simple model that is known that will sufficiently describe sea spike events. This study also concluded that low grazing angle responses are more likely to contain sea spikes than higher grazing angles. Holiday et al [22] also concluded that multipath interference between the incident field and the field reflected from the front face of the wave seemed to be an important factor in the formation of sea spikes. Trizna also suggested similar conditions in [23]. This study concluded that Brewster angle damping of the VV polarization combined with multipath reflections of the HH polarization contributed to sea spike events, especially at low grazing angles. Ja et al's study [16] investigated a different aspect of low grazing angle scattering. That study discussed the effects of wave features on the Doppler spectra of the backscattering. Ja et al discussed the effects of steep surface features to cause what

2

was called "fast" and "slow" scattering. The fast scattering is usually associated with fast moving scatterers, and the slow scattering is associated with the energy shifted to lower Doppler levels [16]. The Doppler splitting discussed in [16] is also seen in this study and will be discussed.

A common approach to the study of multipath scattering is the application of computational electromagnetic techniques to sample surfaces that model breaking waves. Initially, electromagnetic scattering was calculated using perfectly conducting surfaces with surfaces having only roughness in one dimension [12,17]. As roughness was added and scattering theories became more and more accurate, more complex surfaces were used and surfaces began to be treated with their true finite conductivities [13,15,22,]. The high conductivity of the sea has been modeled at microwave frequencies by impedance boundary conditions [14,15].

In most numerical studies, the scattering from surfaces was found using models that only had the general features of an actual breaking wave. While these studies were useful in confirming elements of the existing models, much of the detail that is shown in experimental results is lost. Recently, however, more measurements of actual water surfaces have been used in place of models. These surfaces are usually generated in a wave tank to model certain sea conditions. The most common conditions modeled in wave tanks are plunging and spilling waves that are gravity driven and plunging and spilling waves that are wind driven [13]. In existing studies there have been no simultaneous experimental measurements made along with the surface measurements.

The purpose of this investigation is to study the accuracy of the numerical modeling of electromagnetic scattering from breaking waves measured in a wave tank

3

versus the actual scattering measured by a radar system. The numerical method used in this study is the MM/GTD approach described by West [15]. This method uses the moment method (MM) to find the scattered field from a rough surface that has infinitely long planar extensions added to the end. The geometric theory of diffraction (GTD) is then used on the infinite extensions to correctly model the unknown current on the extensions. This is done to eliminate erroneous edge diffraction results that are given when only the moment method is used on a finite length surface. The scattering calculated in the study will use the impedance of sea water for each of the surfaces in order to more closely model the ocean surface. The main focus of the research was to compare the numerically modeled calculations of scattering from the individual surfaces with those of the experimental measurements in order to confirm that errors are not introduced by either the physical surface measurements or by the numerical electromagnetic model.

This work was applied to waves generated and measured in a wave tank. Dr. James Duncan of the University of Maryland generated both plunging and spilling waveforms for use in numerical electromagnetic calculations. These waves were generated in his wave tank and were captured using a high-speed movie camera that traveled along with the wave as it moved down the wave tank [3]. Simultaneously, Dr. Mark Sletten of the Naval Research Laboratory made measurements of the radar backscatter using a radar antenna that was mounted on a carriage above the tank. This carriage moved at approximately the same velocity as the wave's propagation speed. These measurements will be used to confirm the accuracy of results of current numerical methods.

CHAPTER TWO

ELECTROMAGNETIC THEORY

The numerical electromagnetic scattering calculations in this study were performed using the hybrid moment method/geometrical theory of diffraction (MM/GTD) technique initially developed by Burnside for perfect electric conducting (PEC) wedges [2] and then applied to rough surfaces by West [16,17]. This study used code that was previously developed for similar applications by investigators at Oklahoma State University.

West further developed the hybrid MM/GTD technique for application to finite conductivity surfaces using impedance boundary conditions [15]. In this technique, the moment method (MM) is applied to integral equations that relate the known incident field to the unknown surface current on the scatterer, while the geometrical theory of diffraction is used to represent the unknown current on extensions that are added to the original scatterer [15].

Applying the moment method to solve an integral equation causes the integral to be discretized over the range (in this case, the surface of the scatterer) of the integral. At these discrete points, standard MM pulse functions are used to approximate the integral equations. The pulse functions of the MM are chosen in such a way that the electromagnetic boundary conditions are met on average across the entire surface. On the extensions, a single basis function that has been derived from the GTD is used to find the unknown current on each extension.

Using the MM/GTD method requires that the surface be extended to infinity in planar sections that are completely shadowed from the original surface. The reason for doing this is to remove artificial edges that are caused by the truncating necessary to create the original surface (because it is impossible to store an infinitely large surface). These artificial edges in a modeled or measured surface give a non-physical back-diffraction, and using planar extensions allows the use of a single GTD basis function to represent the current on those extensions.

Figure 1 shows a sample surface for which the backscattering could be calculated. This surface is also the region over which the moment method will be used to find the induced current.

FIGURE 1

Surface without Extension

The addition of the extension to the original surface is shown in Figure 2. The solid line represents the original surface, while the dotted line represents the added extension. When adding the extension, care must be taken to insure that the slope of the planar extension is such that it will be shadowed from the original scatterer. This is usually done by smoothly curving the end of the scatterer down to the desired angle. This extension is added automatically by the code previously developed, so more in-depth discussion of the extension will be delayed until Chapter 3. Once the extensions have been added, the surface current on the scatterer can then be found using the hybrid

MM/GTD technique discussed earlier. Advantages of this hybrid technique include the facts that it is computationally efficient, and it requires no illumination weighting window. However, this technique can only be applied to surfaces to which the correct downward extension may be added [12].

FIGURE 2

Surface with Extension Added
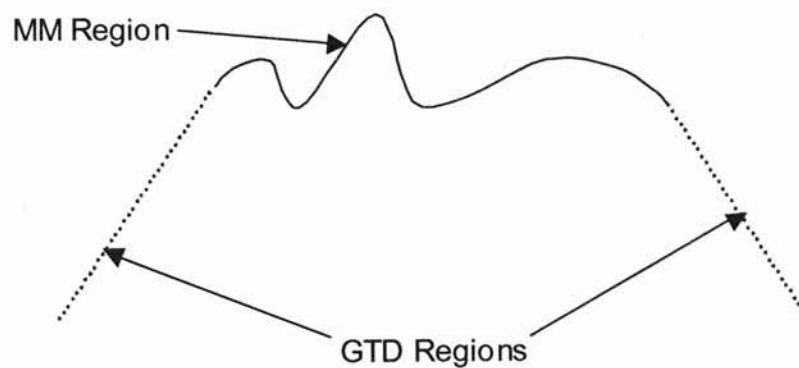
Previous studies by West have shown that the hybrid MM/GTD approach produces results that are consistent with accepted models of sea spike scattering such as the multipath model and the Brewster angle damping model [15].

CHAPTER 3

SURFACE PROFILES

The surfaces used in this study are actual water surfaces that have been created and measured in a wave tank. Not only were these surfaces measured for their dimensions, but they were also electromagnetically illuminated in the 6-10 GHz range. The results of the electromagnetic illumination were recorded and analyzed in order to study sea spike events and to measure the Doppler spectra. These measurements were made so that numerical techniques could be compared to determine the accuracy of those techniques.

As mentioned, Dr. James H. Duncan and Dr. Mark Sletten were responsible for the wave tank generation and measurement of the wave. Dr. Sletten was responsible for the radar measurements, while Dr. Duncan was responsible for the actual wave generation. These experiments were conducted at the University of Maryland in College Park, Maryland. Generation of the waves is described by Duncan *et al* [3].

The waves in the wave tank were generated by creating a packet of waves with different frequencies. Since water wave propagation is dispersive, the crests of the packet converged to produce either a spilling or plunging wave as the packet moved down the tank, depending on the amplitudes of the initial waves [3]. According to Duncan, linear deep-water wave theory was used to generate the wavemaker motion and predict its movement in the tank.

In the set of wave tank measurements taken, two types of waves were modeled. The first, a spilling wave, is a lower energy wave that does not form a jet during

8

breaking. The second, a plunging wave, has more energy and forms a jet that collapses down the front face of the wave.

The wave profiles were captured by mounting a high-speed video camera on an instrument carriage that moved with the wave as it traveled down the wave tank [3]. A laser sheet was used to illuminate the water for resolution of the surface. The frame rate used for this experiment was 250 frames/second. Each of the profiles used in this experiment was detected from an individual video frame of the experiment.

FIGURE 3

Spilling Wave
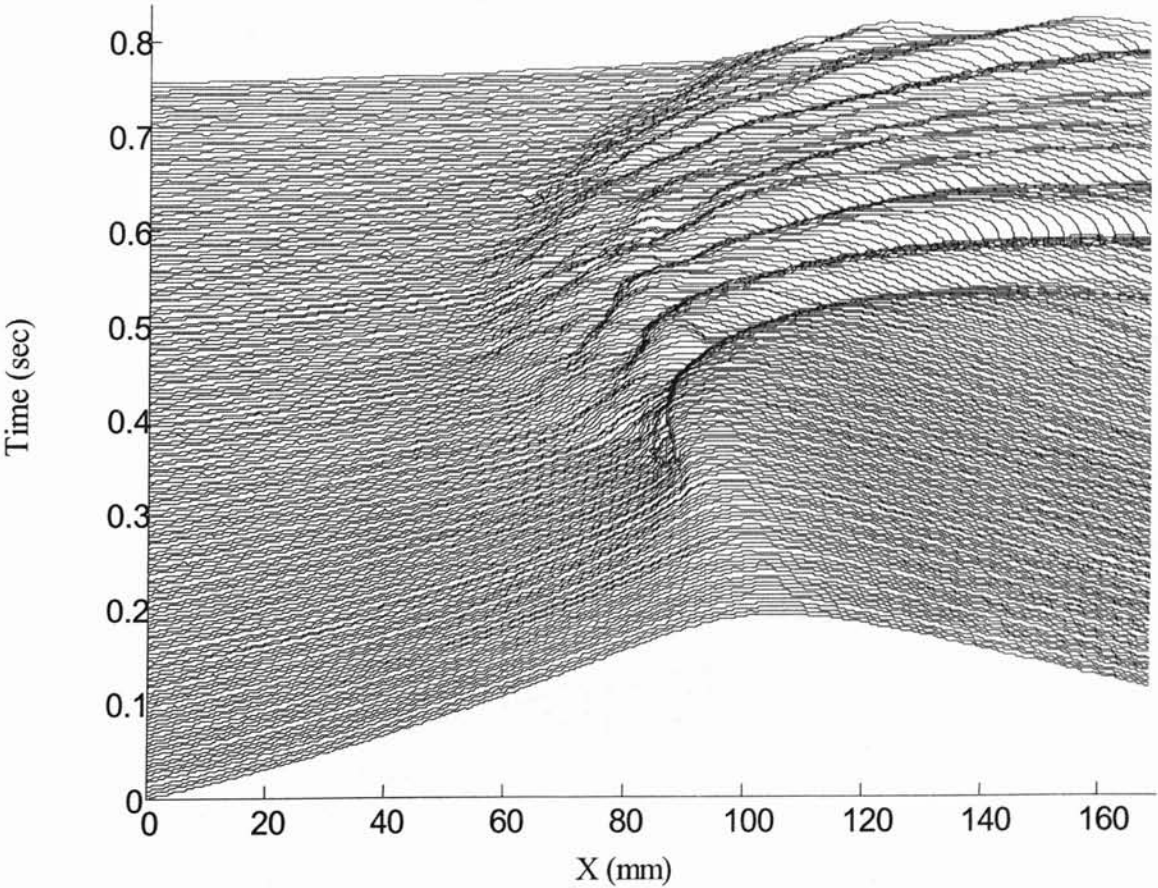
The surface profiles used in this study were created by digitizing the individual frames to create each of the individual wave profiles. The resolution of each image is approximately 1300 by 800 pixels. This process is described in more detail in [3].

Figure 3 shows the complete surface profile of the spilling wave. This profile is comprised of 189 individual surfaces that were captured at a frame rate of 250 frames/second. From Figure 3, it can be seen that this wave builds up to a crest and then dissipates with out a plunging event occurring. The spilling wave's front face is steepest between 0.2 and 0.3 seconds, which is where we expect to see a sea spike event occur.
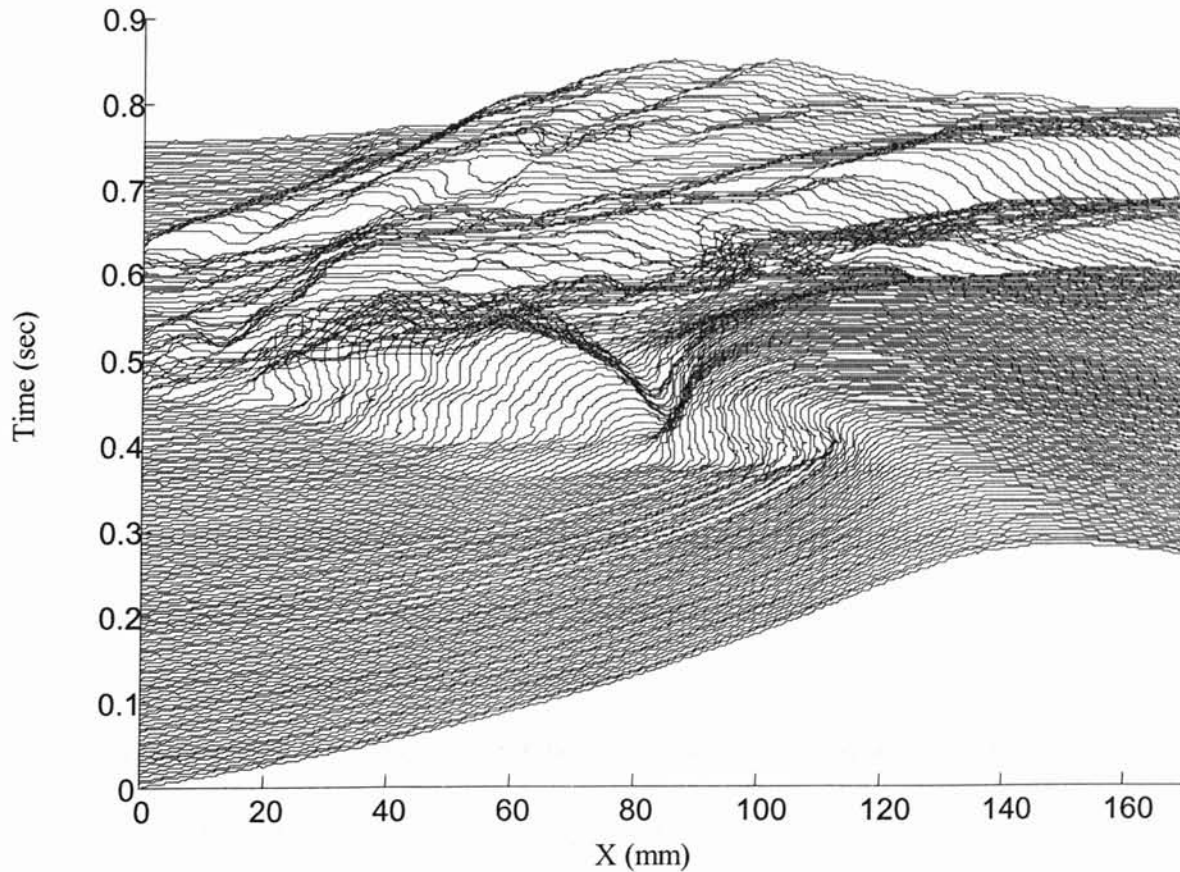
FIGURE 4

Plunging Wave

Figure 4 shows the time history of the plunging wave. It is also comprised of 189 individual surfaces captured at a frame rate of 250 frames/second. This is a much more energetic wave with a jet being formed between 0.2 and 0.3 seconds into the profile. It is important to note that because of the placement of the video camera, the imaging system is unable to resolve the surface details underneath the jet, so there is some unavoidable distortion during this time. In the past sea spikes have been observed that appear to correspond to breaking events of this type. The radar measurements from the experiment indicated that a sea spike is present during the time of breaking, and we hoped to numerically simulate the same results.

As seen in the previous two figures, the digitizing process introduced small pixelization errors and added some very small-scale roughness to the waves. This small amount of noise is electromagnetically small so it does not directly introduce significant backscattering. However, the noise can affect the addition of the infinite extensions needed for the application of the MM/GTD approach. The automatic extension code first adds a short curved section of surface to slope the infinite planar extensions downward at a sufficient slope so that they are shadowed everywhere from the original scattering surface. The slope of the surface must be continuous in this range to minimize the artificial back-diffraction introduced by the extension. The pixelization noise, shown for a specific surface profile in Figure 5, gives erroneous surface slopes at the end points, confusing the automated extension process. The axes units of Figure 5 are the electromagnetic wavelength at 10 GHz, which is 3 cm. To insure that a realistic extension is added, the slopes at the end points were approximated from the average

11

surface slope over the last 15 points of the data set (which is a distance of approximately 0.2 λ).

FIGURE 5

Unaltered Surface Profile
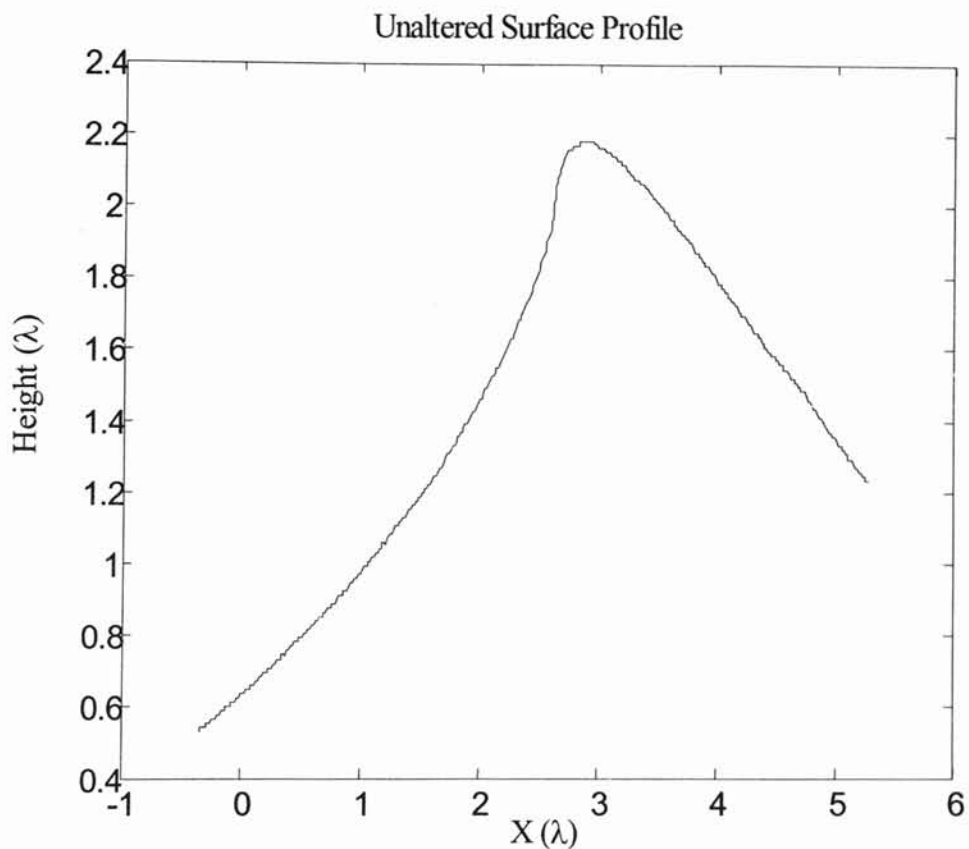
Figure 6 shows the results of adding the MM/GTD extensions needed for a sample profile. The solid line represents the original surface and the dotted line represents the added extensions. The added sections have a radius of curvature of 10 λ, which is large enough to avoid any significant diffraction contributions from discontinuities in the second derivative of the surface. The planar sections of the extension were angled down at 50° below the horizon.

FIGURE 6

Profile with Extensions Added
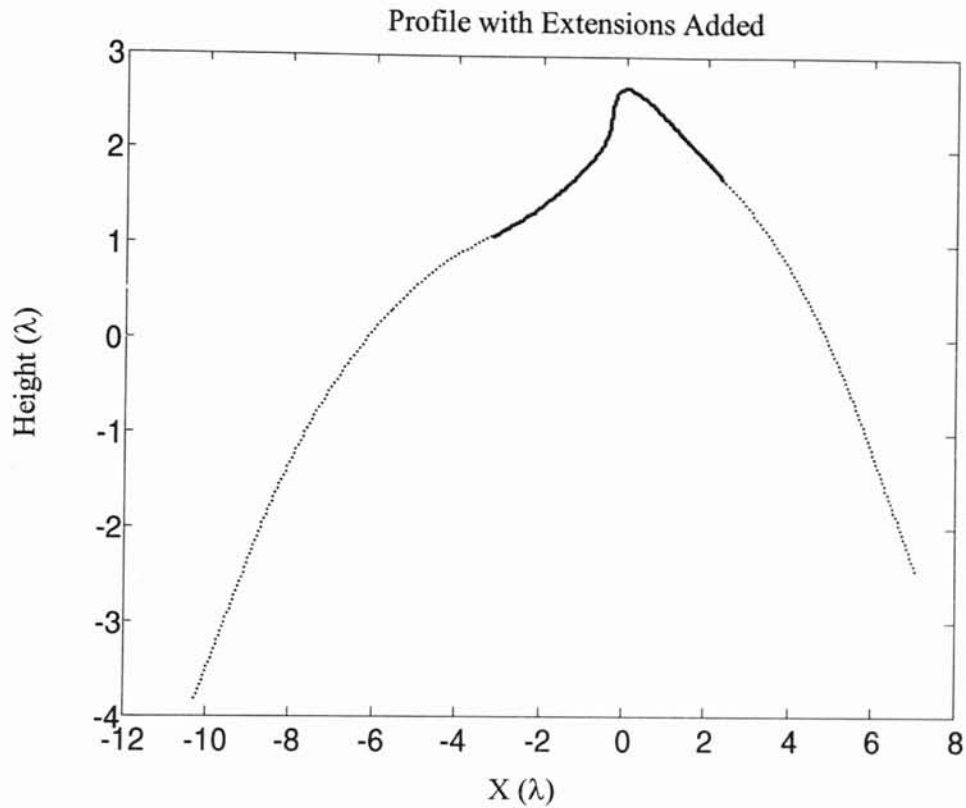
Figure 7 shows another effect of the automatic surface processing routine. The MM/GTD code requires that the surface be sampled every $\lambda/20$ along its length. This distance, however, is greater than the spacing that was actually provided in the original digitized surface profiles. Because of this, the automatic surface processing code resampled the surface at $\lambda/20$ and the other points were discarded. This process tends to smooth the surface considerably, as is shown in Figure 7. The view in Figure 7 shows a view of only the peak of an individual surface. This is done to give an idea of the small scale of the roughness and the amount of smoothing that actually takes place. The solid line represents the original surface, and the dotted line represents the smoothed surface. The scale in this figure is given in terms of electromagnetic wavelength at 10 GHz.

13

FIGURE 7

Smoothed Profile vs. Rough Profile
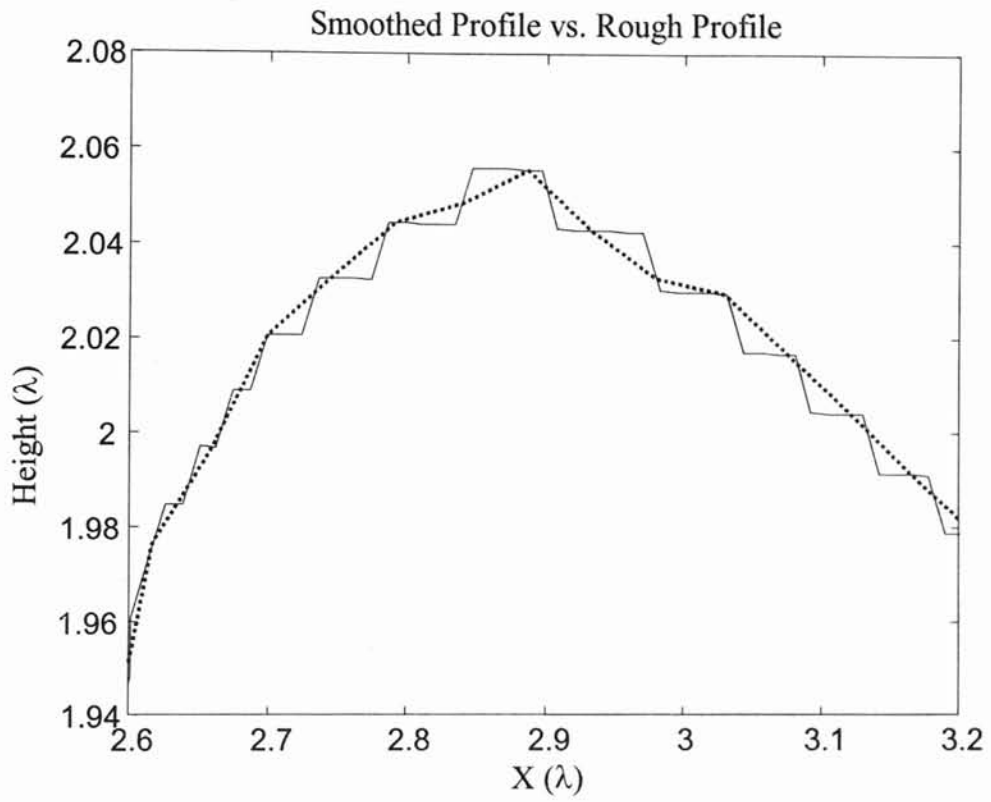
CHAPTER 4

RESULTS

This chapter contains the numerical results from simulation in the form of radar cross-section (RCS) measurements and their associated Doppler spectra. These theoretical results will then be compared with experimental measurements to demonstrate the validity of the numerically modeled results. From results gathered, we will show that numerical simulations applied to measured surfaces can accurately predict the measurement provided that the experimental set-up is fully characterized and accurately represented in the numerical code.

Numerical calculations were first made using a plane wave illumination. This represents the illumination expected for breaking waves in the open sea and allows the overall comparison of the numerical results with previously existing experimental results. Illumination more closely approximating the NRL experimental conditions is then considered. Both the radar cross-section (RCS) and Doppler shift of the scattering from both the spilling and plunging breakers will be considered. All results shown here correspond to an electromagnetic frequency of 10 GHz.

Figure 8 shows a rough sketch of the experimental setup used by Dr. Sletten. The distance between the antenna and the wave crest and the wave crest itself are both drawn to scale. There is a distance of 1.57 meters from the peak of the wave crest to the antenna. The antenna is pointed down at an angle of 14 degrees below horizontal (i.e. a grazing angle of 14 degrees). Because of the antenna pattern used, only the crest of the wave is visible to the antenna in the experiment.

FIGURE 8

Experimental Setup
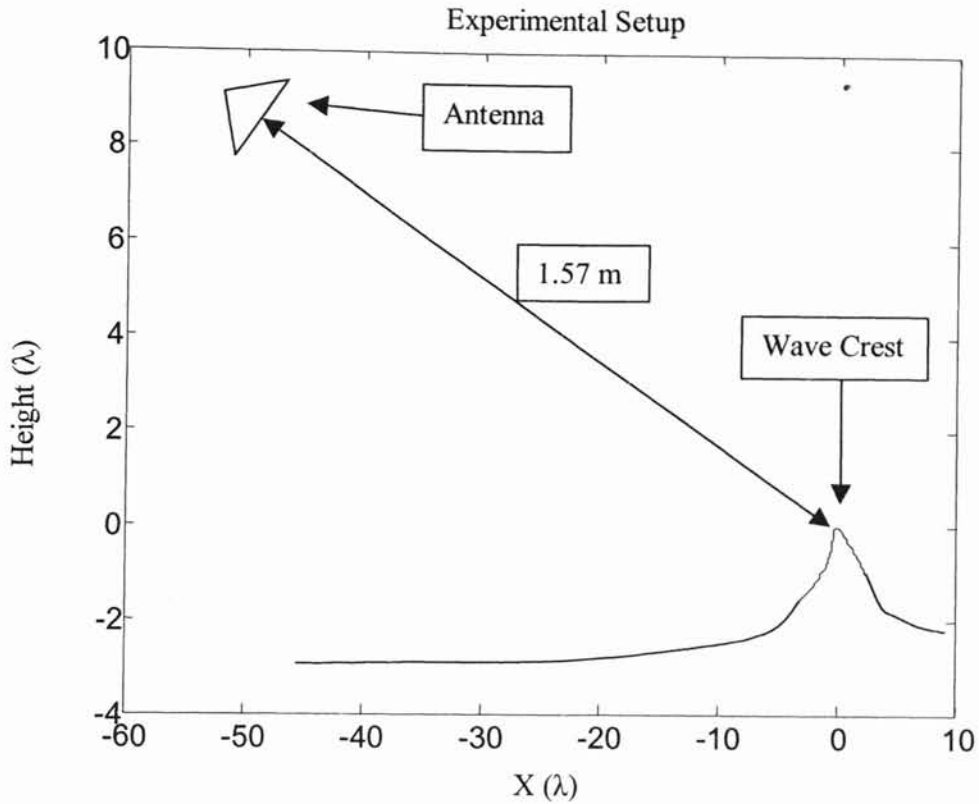
Spilling Wave Radar Cross-Sections

Figure 9 shows the RCS of the spilling breaker that was measured in the wave

tank experiments by Sletten. This figure clearly shows that an HH/VV ratio of greater

than 1 occurs between approximately 0.15 and 0.35 seconds. At its largest, the ratio of

HH/VV scattering is in the range of 8-10 dB. Comparing the time of the sea spike to the

surface profile, we see that this apparent sea spike does indeed occur at the time when the

wave's front face is the steepest. We also notice that there are much smaller events with

HH/VV greater than 1 occurring between 0.35 and 0.45 seconds, none of which are as

long lasting as the initial response measured. Each of these appears to correspond to the

formation of large features on the crest. After 0.45 seconds, the HH scattering drops

16

below the VV level permanently. The lowest levels have been truncated by the noise

floor of the processor. In this period the relative maxima still correlate with surface

features. Throughout the experiment, the VV backscattering remains strong, dropping

only a few dB on average after the initial crest collapse.

FIGURE 9

Experimental Spilling Wave RCS vs. Time

RCS at 10 GHz, File umd90510.ils, Frames 719-906

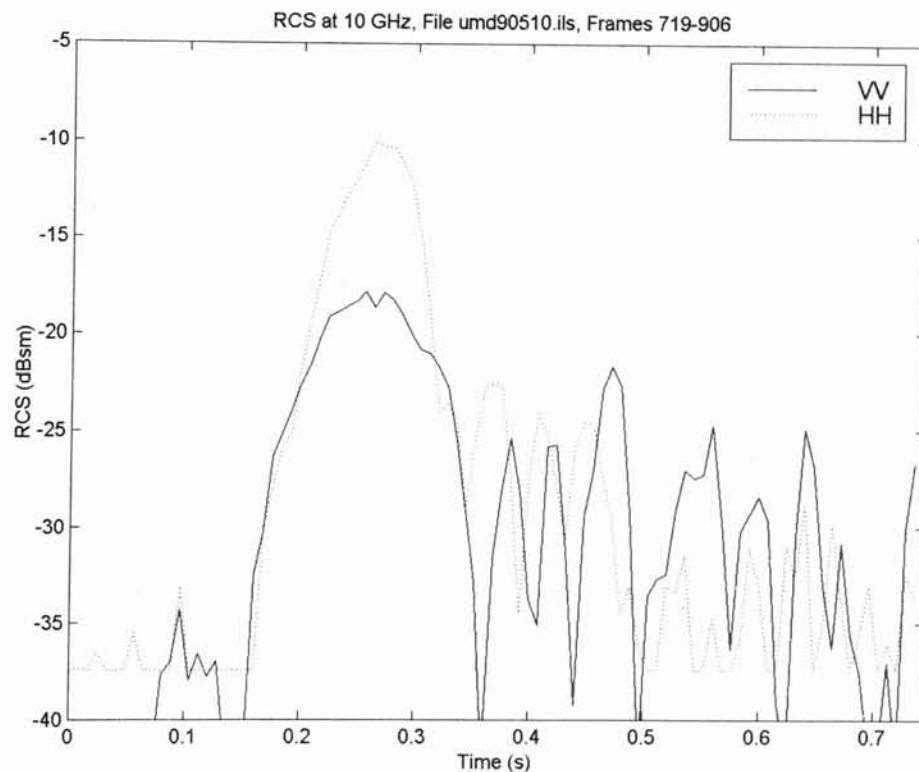Figure 10 shows the numerically calculated RCS of the spilling breaker with

plane wave illumination at an incidence angle of 76 degrees (14 degrees grazing). The

dotted line represents the HH polarization, and the solid line represents the VV

polarization. There are several obvious major differences between the experimental

results of Figure 9 and the numerical results of Figure 10. The first is that the overall

17

HH/VV ratio is much lower in Figure 10. The peak HH/VV is only 3 dB and has a shorter duration. The numerical results also oscillate more rapidly after the crest collapses at 0.27 seconds. However, despite these differences, there are some common features between the experimental and numerical results.

FIGURE 10

Plane Wave RCS Scattering vs. Time for the Spilling Wave
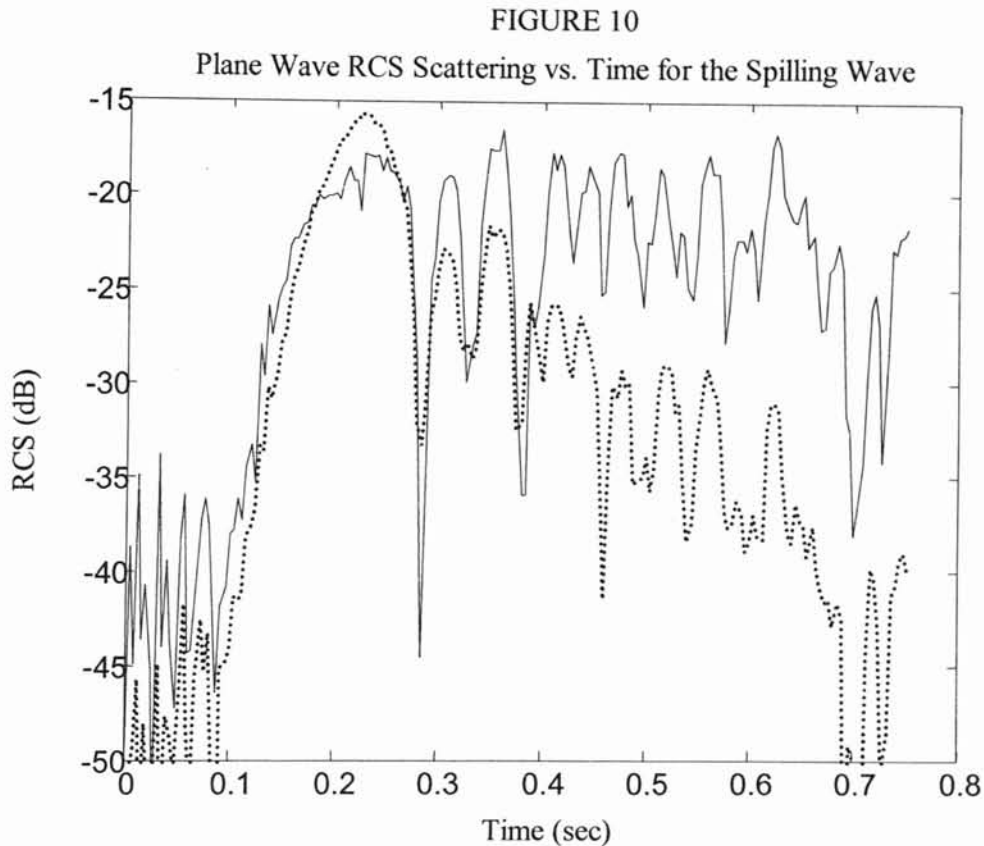
First, the overall trends of the responses are the same. VV polarization becomes strong as the wave first crests, and remains approximately the same magnitude through the remainder of the measured time. HH, on the other hand, is dominated by the initial response. The HH response then continuously drops as the wave evolves. Second, the numerical calculations respond to the same features as the experiment. Peaks around 0.4 and 0.5 seconds in the experiment are reflected in the calculations. In some cases, single

peaks in the experiment are reflected by multiple peaks in the calculations. This is not too surprising, however, because the surface measurements are limited to a single plane. Isolated features that are of limited width on the wave appear as infinitely wide in the calculations and have a very large effect. On the actual surface the limited extent gives less effect, so the multiple peaks average out into single peaks.

It is important to point out that while the values on the vertical scales of Figures 9 and 10 are different, they still cover the same range (35 dB). This is a result of the differences between the three-dimensional (experimental) and the two-dimensional (calculated) measurements. When comparing the two responses, it is more important to note the relative magnitude of HH to VV rather than comparing the magnitudes of Figure 9 with those of Figure 10. These differences will also be seen in later plots of experimental and calculated responses for the plunging wave.

Overall, comparison between the plane wave illumination numerical calculations and the experimental measurements showed good agreement in all areas except that of the HH/VV ratios. This was first believed to be an effect of multipath scattering. However, this could not be confirmed because only the wave crests were recorded on video camera during the experiment. Numerous front face approximations were added to the waves, but they all failed to improve the agreement between the plane wave simulation and the experimental measurements. These failures prompted a complete measurement of the antenna pattern by Dr. Sletten at NRL. The result of these measurements was to prove that the wave crests were not in the far-field region and that the antenna pattern was different for the HH and VV polarizations. Also, the numerical work showed that the antenna was focused on the wave in such a manner that the peak of

the antenna beam was not focused on the peaks of the wave crests. Comparison of the

profile measurements and radar cross-section measurements and calculations also shows

a slight temporal offset that has recently been determined to be a result of misregistration

between the clock used by the profile measurement system and the one used by the radar

system [28]. This temporal difference is also evident in the plunging breaker cases.

FIGURE 11

Sample Plot of Antenna Pattern on Surface

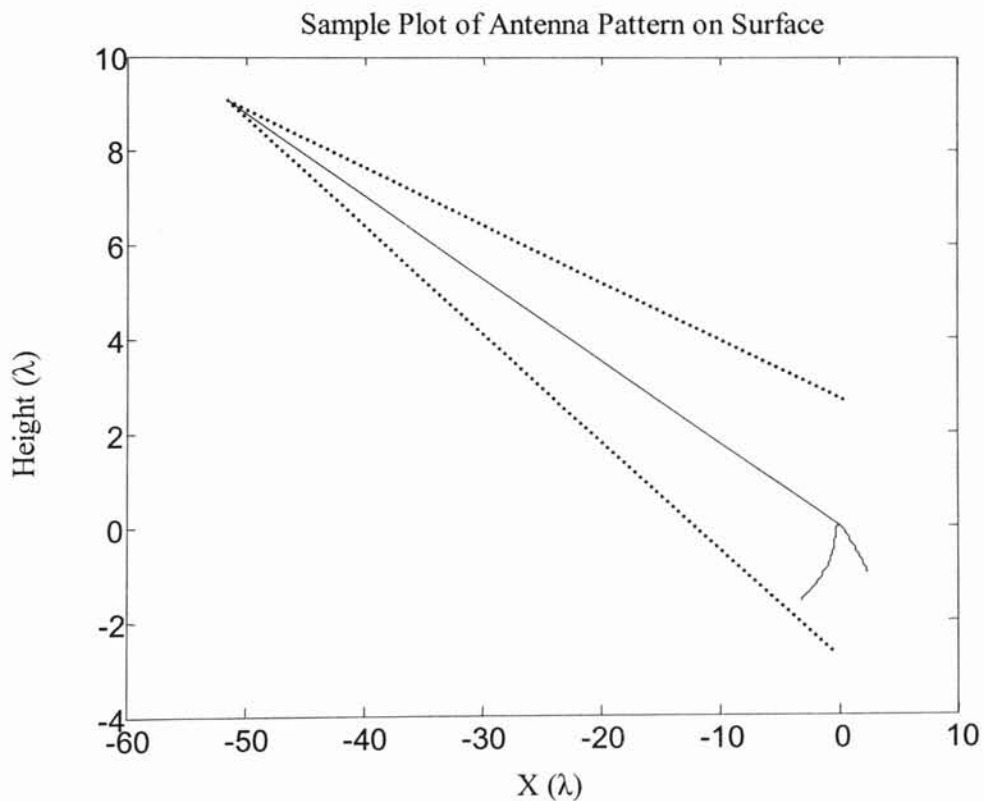Figure 11 shows a sample of what the antenna pattern looks like as it falls on an

individual surface at 14 degrees grazing. The solid center line of the pattern represents

the peak of the antenna beam, while the two dotted outside lines represent the –6 dB

points in the antenna pattern. The total beam width is approximately 6 degrees, with the

beam width being approximately 12 cm across when its center encounters the peak of the

surface. The units on the figure are given in term of wavelength at 10 GHz. After several

tests, it was determined that placing the peak of the wave 12 cm below the peak of the

beam gave the best agreement between the numerical and experimental measurements.

This configuration is used for all following calculations.

FIGURE 12

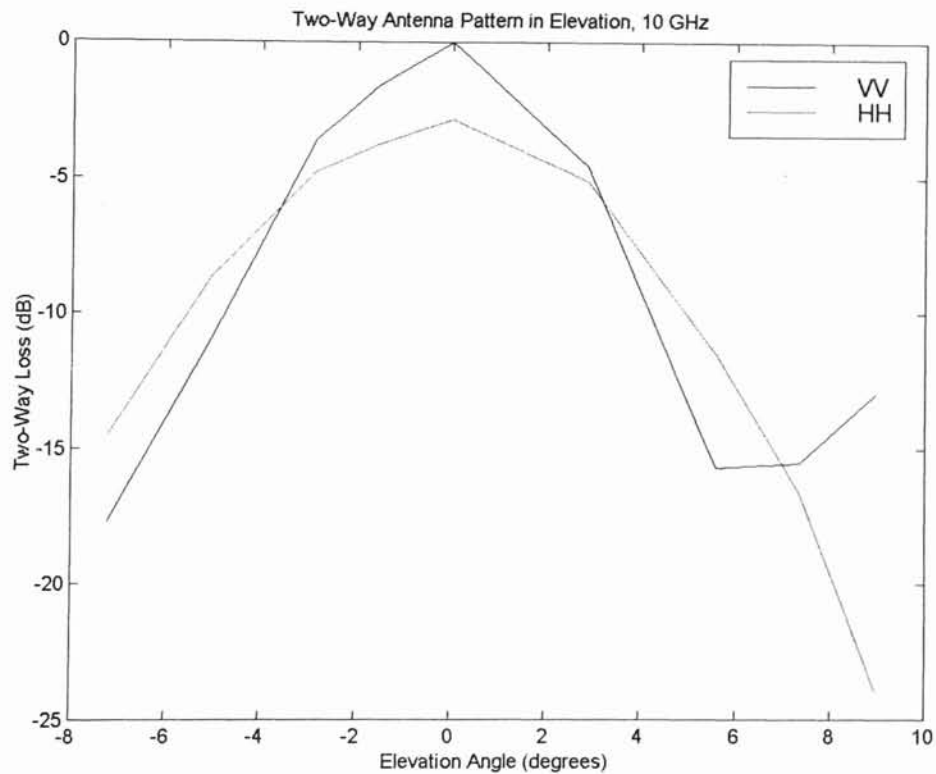Figure 12 shows the actual radar pattern that was measured by Sletten in the wave

tank experiments. This figure represents measurements taken of the antenna pattern for

both the VV and HH polarizations. The line representing the VV polarization peaks at 0

dB at 0 degrees elevation, while the HH polarization peaks at approximately –3 dB at 0

degrees elevation. These patterns were included in the numerical illumination

simulations, and the actual pointing of the patterns was adjusted until the best agreement

between the numerical and experimental results were achieved.

FIGURE 13

Antenna Pattern RCS Scattering vs. Time for the Spilling Wave
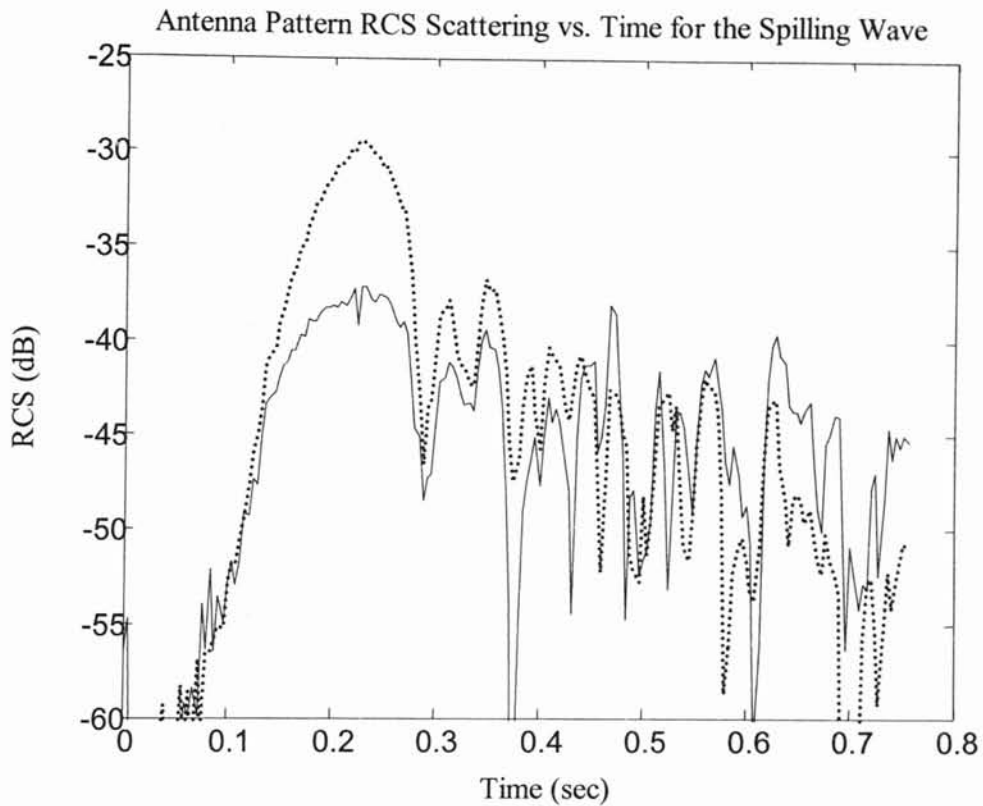
Figure 13 shows the numerically calculated scattering cross-sections of the

spilling breaker when the measured antenna beams were considered. The dotted line

represents the HH scattering, while the solid line represents the VV scattering. The

HH/VV ratio matches the experimental results in Figure 8 much better throughout the

measurement period. This gives greater evidence that the numerical simulation gives the

same responses to the same wave features as the experimental measurements made by

Sletten.

Plunging Wave Radar Cross-Sections

Figure 14 shows the experimentally calculated RCS scattering from the plunging wave. In this figure the HH response exceeds the VV response over most of the measurement period. Comparing this time scale to that of the plunging wave profile history in Figure 4, we see that again peaks in the response occur in conjunction with the formation of a plunging jet or other steep features on the wave's surface.

FIGURE 14

Experimental Plunging Wave RCS vs. Time

RCS at 10 GHz, File umd90111.ils, Frames 725-914
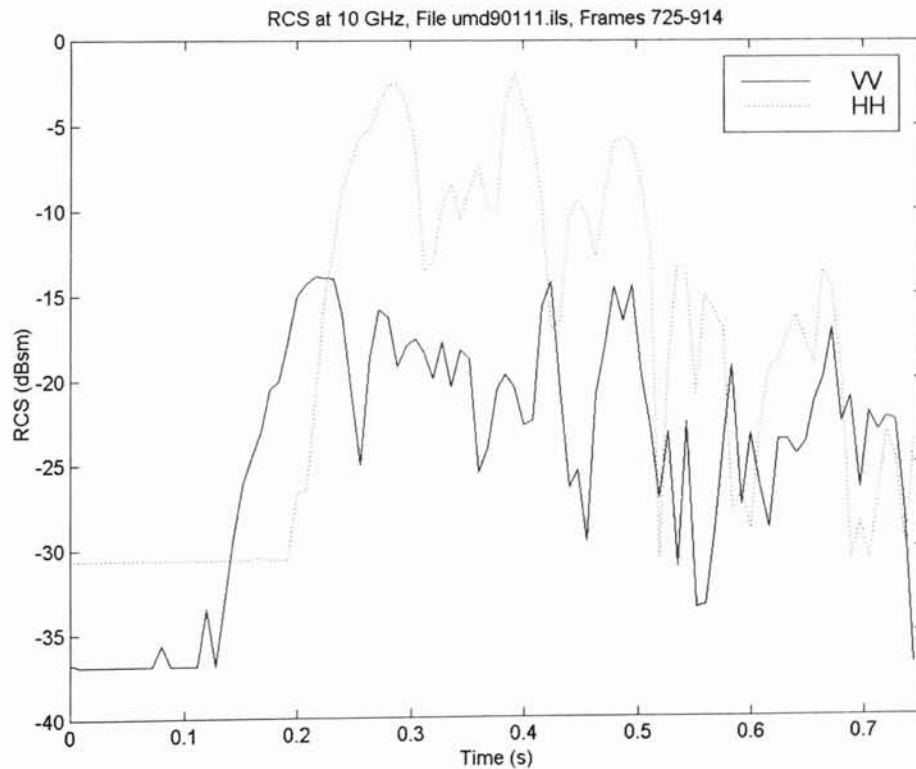
Also, since steep features remain on the surface much longer than with the spilling wave, the HH response remains strong until later in the breaking process. Finally, the initial

HH peak at 0.28 seconds corresponds to a minimum in VV. This behavior was predicted numerically in West [14].

FIGURE 15
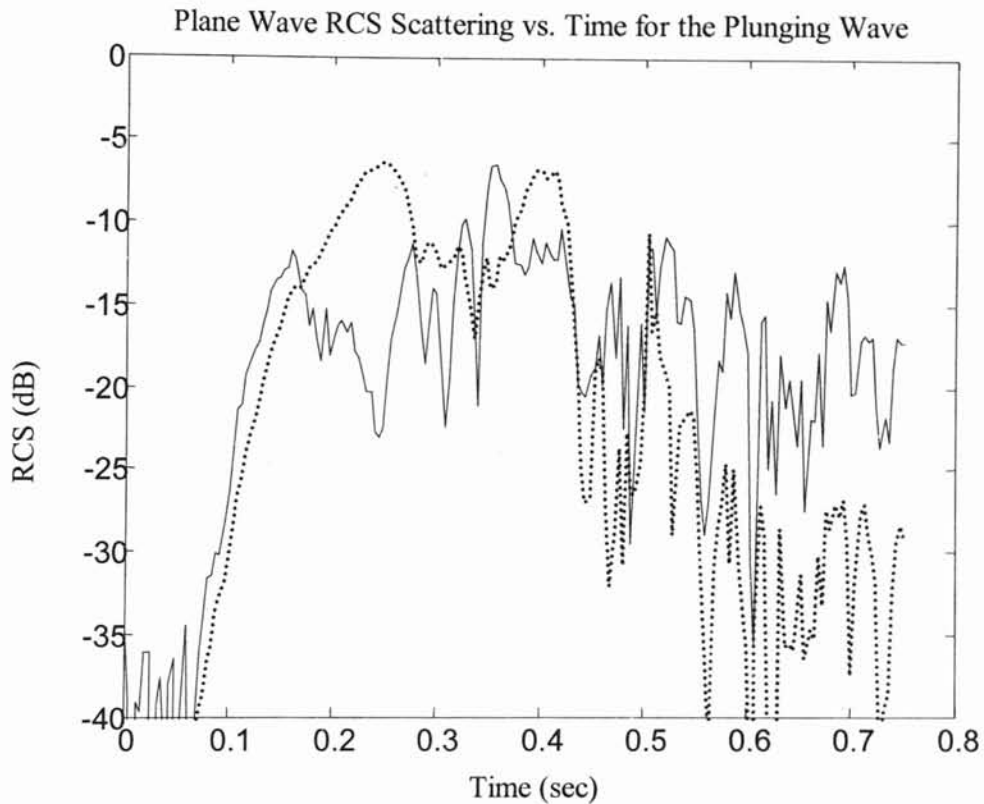
Figure 15 shows the numerically calculated scattering results when plane wave illumination was modeled on the plunging wave's surface. The dotted line represents the HH scattering, while the solid line represents the VV scattering. Again, as in the spilling wave case, we see that the HH/VV ratio is much lower than in the experimental results. However, the signal does show relative maxima at the same relative times as the experimental results, indicating that both are again responding to the same features.

FIGURE 16

Antenna Pattern RCS Scattering vs. Time for the Plunging Wave
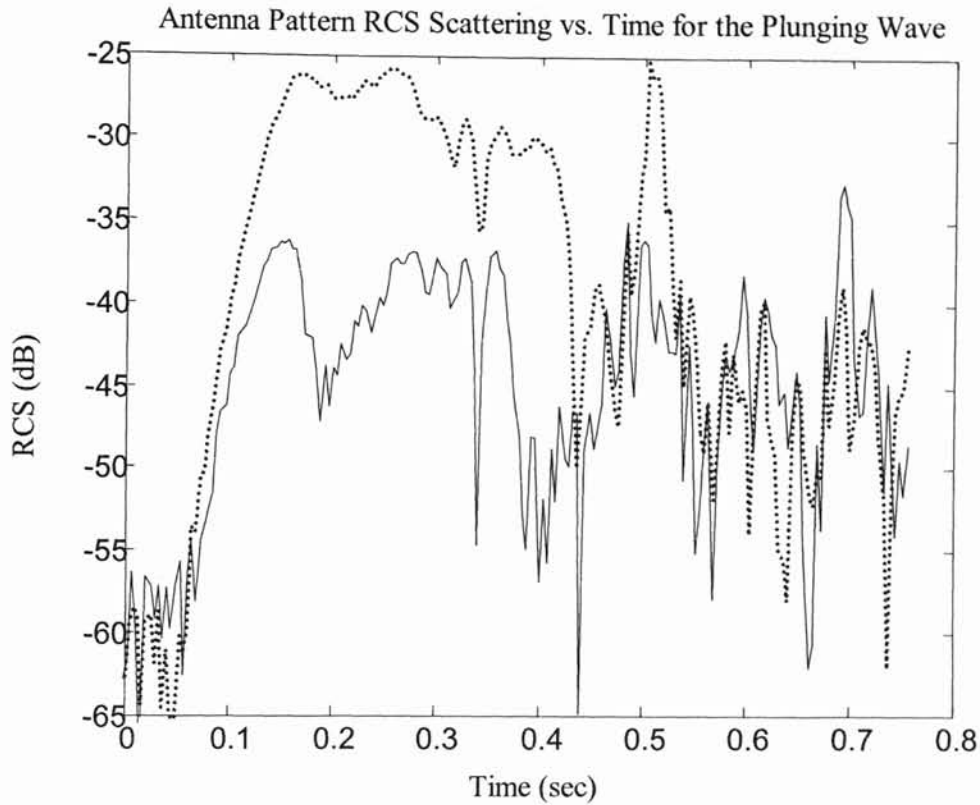
Figure 16 shows the RCS scattering calculated when adding the same antenna pattern effects as used with the spilling breaker. The dotted line represents the HH scattering, while the solid line represents the VV scattering. Figure 16 shows that the HH/VV ratio now matches the measurements much better than when plane illumination was used. Some of the details in the individual feature responses have been lost, however, indicating that either the antenna pattern or its spatial representation is not ideally represented. Other than the antenna pattern inaccuracies and the temporal offset discussed earlier, the agreement achieved between the numerical calculations and experimental measurements shows that the hybrid MM/GTD method may be used to accurately represent expected measurements from a water surface.

25

Experimental Doppler Shifts

In addition to the RCS scattering calculations that were made, calculations of the Doppler spectra and spreading were also made. These calculations were made using FFT techniques with the complex calculated RCS scattering using the method described by Ja et al [16]. The results that follow show that the numerical measurements for the plane wave illumination have good agreement with the experimental measurements. As will be shown in more detail later, responses in the Doppler spectrums may be correlated with specific surface features on the waves. It will also be shown that the HH responses consist only of fast Doppler shifts, while the VV responses consist of both fast and slow Doppler shift.

Because the radar measurements were made from a carriage that was moving at the same speed as the wave, the frame of reference in this section is such that a positive Doppler shift indicates that the wave or wave feature is moving faster than the carriage, and a negative Doppler shift indicates that the wave or feature is moving slower than the carriage.

Figure 17 shows the HH Doppler measurements made on the spilling wave during the experiment. The magnitude scale in Figures 17 through 20 ranges from –13 dB (black) to –1 dB (white). These figures were normalized to the peak response of each figure. Figure 17 shows that the spilling wave has its largest HH Doppler response from 0.2 to 0.25 seconds and from 0 to 10 Hz. Comparing Figure 17 with Figure 3 shows that the peak of the Doppler response occurs at the same time as the steepest face of the spilling wave. After the initial response in the HH, the Doppler response rapidly decays and is too low to be of any consequence after 0.45 seconds.

FIGURE 17

Experimental Spilling Wave HH Doppler Shift

HH Doppler Spectrum; file name ur-d90510. ls; Frames 719-930 10 GHz
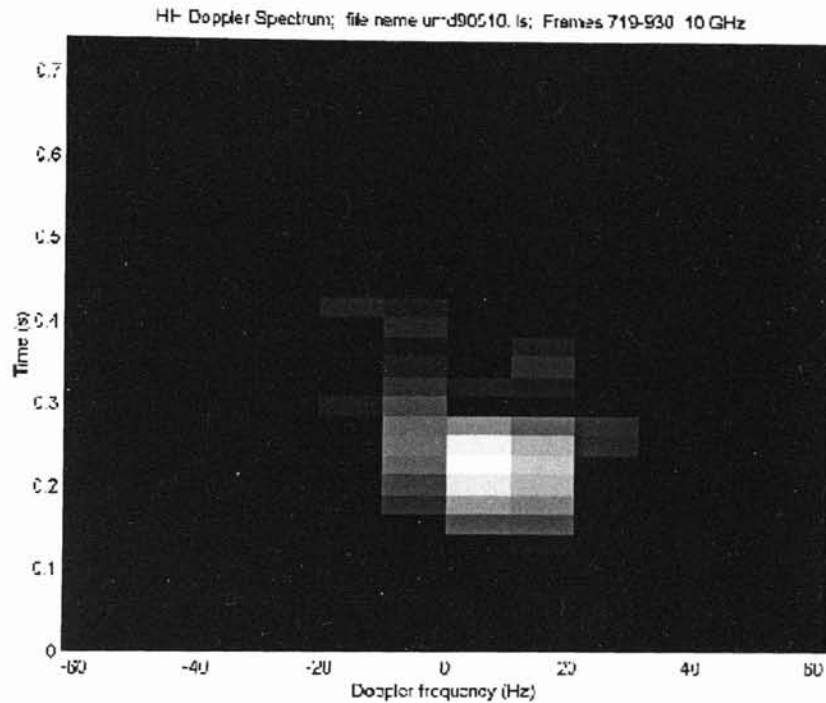
Figure 18 shows the VV Doppler shift measured from the spilling wave. Again, the largest Doppler response occurs at the same time as the steepest face of the spilling wave appears. The first, largest response occurs between 0 and 10 Hz from 0.2 to 0.25 seconds in Figure 18. There is a second, lower response that peaks between 0.4 and 0.45 seconds at Doppler frequencies of −10 to 10 Hz. There continue to be smaller responses as the wave collapses that move farther into the negative Doppler frequency range. Comparison of Figures 17 and 18 with Figure 3 indicates that the spilling wave is initially moving faster than the camera, but after it reaches its peak it simply collapses and slows down.

FIGURE 18

Experimental Spilling Wave VV Doppler Shift

VV Doppler Spectrum; file name umd90510.ils Frames 715-930; 10 GHz
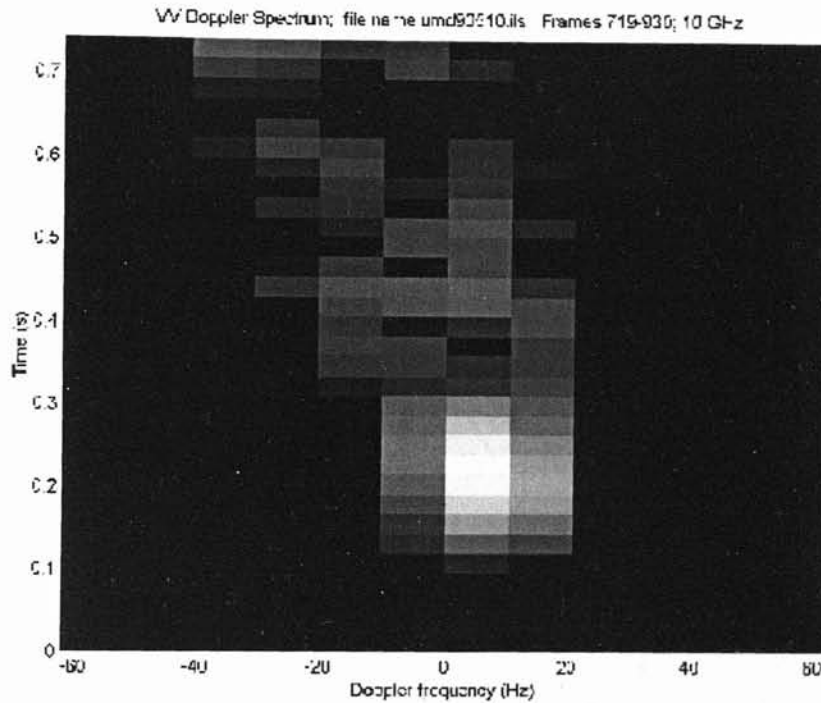
Figure 19 shows the HH Doppler shift that was measured from the plunging

wave. This figure shows a much more energetic wave, with almost all of the responses

occurring in the positive Doppler frequencies. The first and largest peak of the HH

polarization occurs between 20 and 30 Hz around 0.3 seconds into the wave. Comparing

Figure 19 with Figure 4 shows that the largest response occurs at the same time as the jet

begins to appear and move down the front face of the wave. There is also a second,

smaller peak in the HH Doppler response that occurs around 40 Hz at 0.4 seconds. This

second response occurs as the jet collapses down the front face. As the jet plunges down

the front face of the wave, it is moving faster than the wave itself, causing the Doppler

shift to higher frequencies. There is also a smaller, noticeable response that occurs

between 10 and 20 Hz around 0.5 seconds into the profile.

FIGURE 19

Experimental Plunging Wave HH Doppler Shift

HH Doppler Spectrum; file name ur-d90111. ls; Frames 725-930 10 GHz
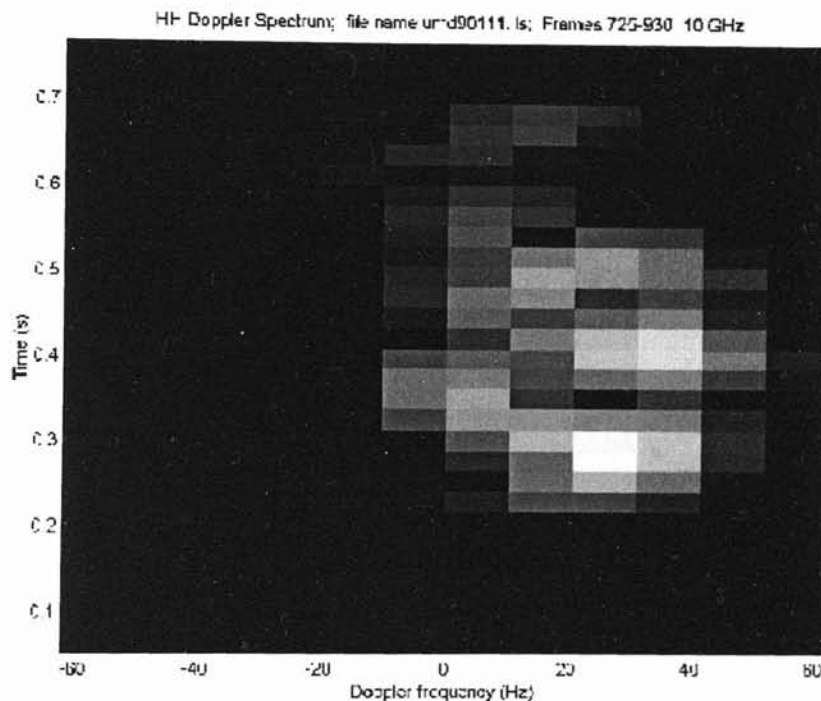
Figure 20 shows the VV Doppler shift that was measured from the plunging

wave. This response also features two main responses and several smaller ones that

occur as the wave collapses near the end of the profile. The first response peaks between

10 and 20 Hz and around 0.2 to 0.25 seconds. The second, lower response occurs

between 20 and 30 Hz around 0.5 seconds. These first two responses also correspond to

the time of formation of the jet and the time of the jet's collapse down the front face of

the wave. Also noticeable are several smaller responses that occur over the range of –40

to 10 Hz between 0.6 and 0.7 seconds. It is these responses that are occurring as the wave surface becomes noisier and loses energy.

FIGURE 20

Experimental Plunging Wave VV Doppler Shift
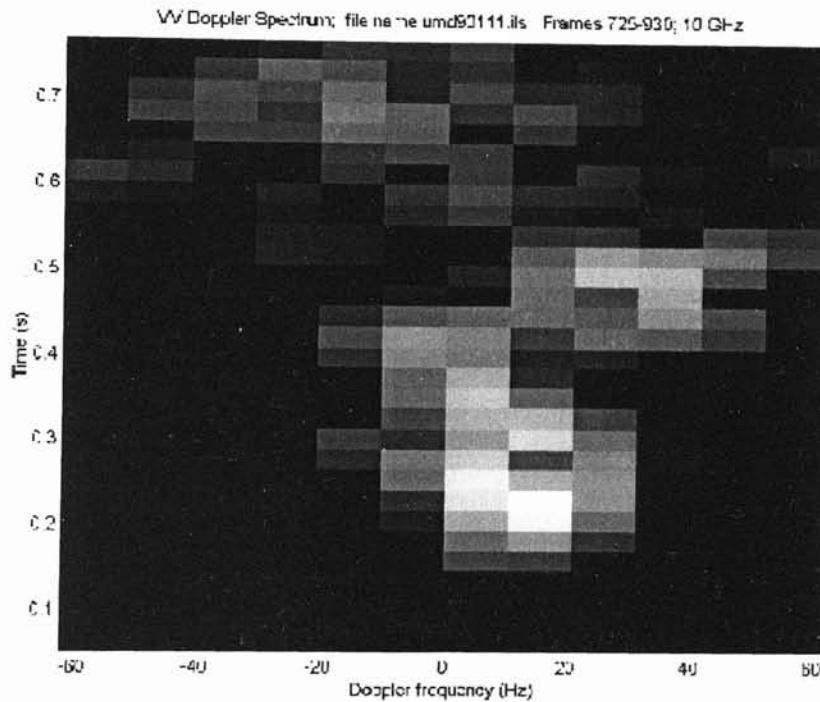
Plane Wave Doppler Shifts

Figures 21 through 24 feature the numerically calculated Doppler shifts for the spilling and plunging waves at both VV and HH polarizations. Each of these figures has been normalized to the highest response of that figure. Figures 21 through 24 focus on the plane wave illumination of the waves. These figures are in the form of contour plots and range from −13 dB (white) to −1 dB (black).

Figure 21 shows the HH Doppler response that was numerically calculated from a plane wave illumination of the spilling wave. Figure 21 shows a peak response occurring from 0 to 10 Hz between 0.2 and 0.25 seconds. This response gradually decreases and moves into the negative Doppler frequencies past 0.35 seconds. Beyond 0.45 seconds, the Doppler responses become so low that they are beyond useful thresholds. Comparison of Figures 17 and 21 shows similar responses to the same features of the spilling wave.

FIGURE 21

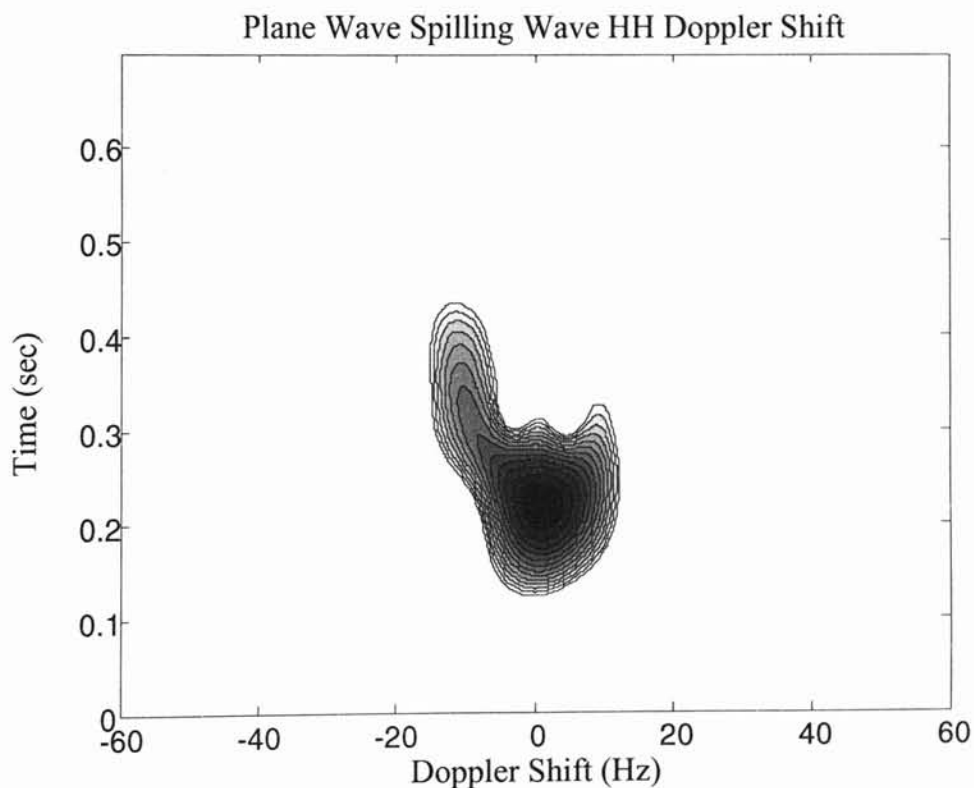Plane Wave Spilling Wave HH Doppler Shift

Figure 22 shows the numerically calculated VV Doppler shift from plane wave illumination of the spilling wave. This figure shows 5 noticeable peaks in the Doppler response. The first and largest response occurring in this figure peaks from 0 to 10 Hz between 0.15 and 0.2 seconds. The second peak occurs from −10 to 0 Hz between 0.3

and 0.4 seconds. The third response occurs from 0 to 10 Hz around 0.45 seconds, and the fourth response occurs around 0 Hz between 0.5 and 0.55 seconds. The final response is the lowest of the five and occurs from –30 to –20 Hz around 0.6 seconds. Comparison with Figure 18 shows similar responses to the same wave features. Comparing Figure 22 to Figure 3 shows that the first peak response occurs as the steepest face of the wave is forming.

FIGURE 22
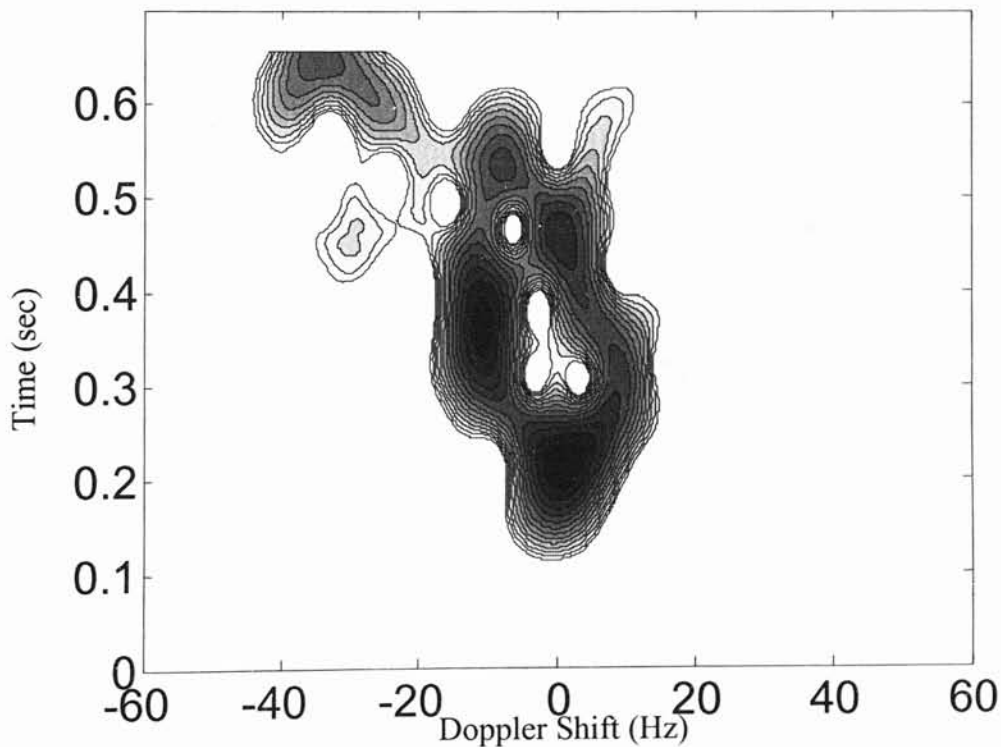Plane Wave Spilling Wave VV Doppler Shift

Figure 23 shows the HH Doppler shift for the plane wave illumination of the plunging wave. This figure shows two peaks in the Doppler response. The first peak occurs from 10 to 20 Hz between 0.2 and 0.25 seconds. The second peak occurs around 30 Hz between 0.35 and 0.4 seconds. Comparison with Figure 19 shows a very similar

32

Doppler response. These figures show the same peak responses to the same features of the plunging wave. Comparing Figure 23 with Figure 4 shows that the peaks in the Doppler response occur as the jet on the plunging wave forms and then collapses down the front face of the wave. There is agreement between Figures 23 and 19 as to the general trends of the magnitude and duration of the Doppler shifts.

FIGURE 23

Plane Wave Plunging Wave HH Doppler

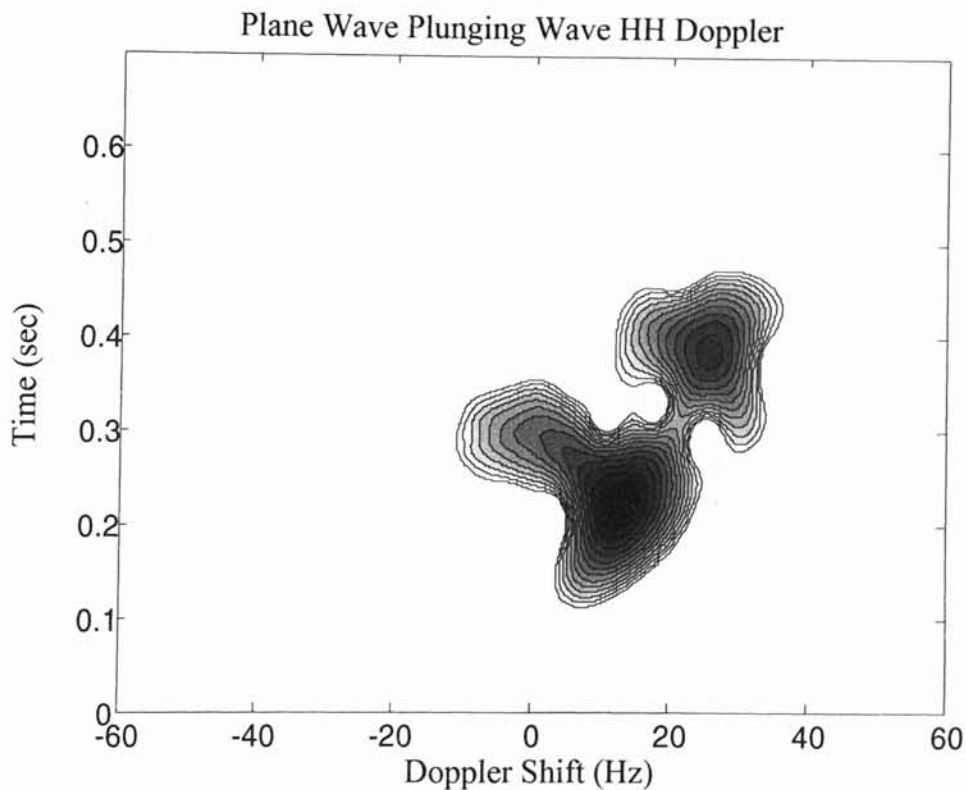Figure 24 shows the VV Doppler shift for plane wave illumination of the plunging wave. This figure shows three larger peaks, with two smaller ones occurring as the wave is collapsing and slowing down. The first peak occurs from 5 to 15 Hz between 0.15 and 0.2 seconds. The second peak occurs from 0 to 10 Hz between 0.25 and 0.3 seconds. The third peak in Figure 24 appears to have the highest response, and it occurs

from 20 to 30 Hz between 0.35 and 0.4 seconds. There are also two smaller peaks which

occur from –20 to 0 Hz between 0.5 and 0.55 seconds. Comparison of Figure 24 with

Figure 20 shows many similarities between the two, but they do not exactly match.

Temporal differences are currently being studied to see if differences are introduced in

the experimental measurements or in the numerical calculations. From comparison it

appears that each figure shows similar responses to the same features of the plunging

wave.

FIGURE 24

Plane Wave Plunging Wave VV Doppler
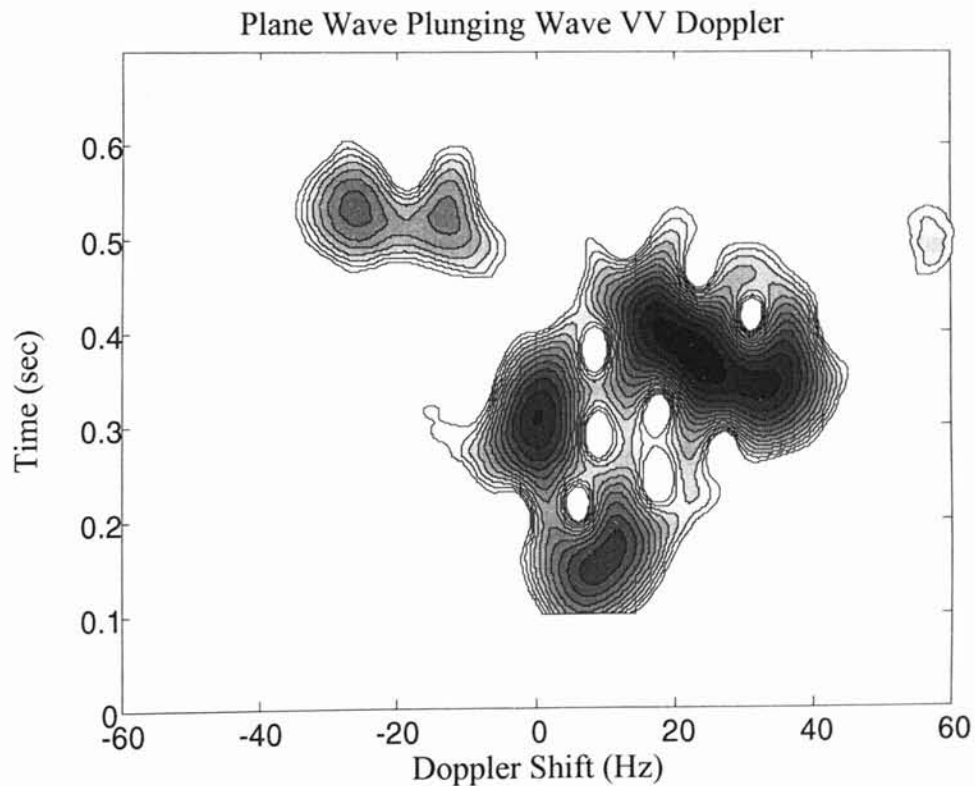
CHAPTER 5

CONCLUSIONS

Electromagnetic scattering from measured water surfaces has been examined.
The surfaces are generated in a wave tank to give two types of breaking water waves,
spilling and plunging. The spilling wave is a wave with less energy that forms a steep
face but does not break down its front face. The plunging wave has more energy and
forms such a steep face that a jet forms and water breaks down the front face at speeds
faster than the wave is traveling.

An instrument carriage traveled with the wave crests, allowing a continuous
measurement of the crest. Frames from a movie of the crest were digitized to give
surface profiles at discrete points in time of the wave's evolution. These profiles were
then used to numerically calculate the RCS backscattering that could be expected from
electromagnetic illumination. For this study a frequency of 10 GHz was used, but the
techniques discussed will work for a wide range of frequencies. Also calculated in this
study were the Doppler spectra associated with the backscattering from each surface
profile. A radar system was also mounted on the instrument carriage that gave a
continuous experimental measurement of the radar cross-section to which the numerical
calculations were compared.

From comparisons of the numerically calculated backscattering and the
experimentally measured backscattering, we see that the hybrid MM/GTD technique
applied to the measured surfaces can be used to provide realistic simulations of
backscattering that can be expected from a sea surface. The numerical calculations

responded to the same surface features as the experiment, and the trends over time at the two polarizations were similar. Differences between the two most likely result because the surface measurements were limited to a single plane and the surface had to be assumed to be uniform in the azimuthal dimension. The actual surface was of course not ideally uniform, so fine detail that appeared in the numerical results can be expected to be missing in the actual measurements. This proved to be the case. Overall, the Doppler shifts showed very good agreement between the numerical and experimental results.

The major difference in the numerical and experimental results was the difference in HH/VV when ideal plane wave illumination was numerically assumed. This mimics the expected effects of the multipath interference proposed by Trizna [23], and initially was thought to explain the observations. However, further experimentation showed that no multipath reflection could occur with the experimental configuration. Instead, it was determined that the antennas used in the experiment were operating in the near field, giving complicated illumination of the crest. When the measured antenna patterns were included in the simulations, much better agreement in HH/VV was achieved. This further demonstrates the utility of numerical simulation in conditions where physical limitations make exact experimental measurements very difficult.

BIBLIOGRAPHY

[1]   Balanis, Constantine A., *Advanced Engineering Electromagnetics*, New York: John Wiley and Sons, 1989, pp. 671-717.

[2]   Burnside, W.C., C.L. Yu, and R.J. Marhefka, "A Technique to Combine the Geometrical Theory of Diffraction and the Moment Method," *IEEE Transactions on Antennas and Propagation*, **vol. AP-23**, pp. 551-558, July 1975.

[3]   Duncan, James H., Haibing Qiao, Vasanth Philomin, and Alexandra Wenz, "Gentle Spilling Breakers: Crest Profile Evolution," *Journal of Fluid Mechanics*, **vol. 379**, pp. 191-222.

[4]   Glisson, Allen W., "Electromagnetic Scattering by Arbitrarily Shaped Surfaces with Impedance Boundary Conditions," *Radio Science*, **vol. 27**, no. 6, pp 935-943, November-December 1992.

[5]   Liu, Yong, Stephen J. Frasier, and Robert E. McIntosh, "Measurement and Classification of Low-Grazing-Angle Radar Sea Spikes," *IEEE Transactions on Antennas and Propagation*, **vol. AP-46**, no. 1, pp. 27-40, January 1998.

[6]   Rino, Charles L. and Hoc D. Ngo, "Numerical Simulation of Low-Grazing-Angle Ocean Microwave Backscatter and Its Relation to Sea Spikes," *IEEE Transactions on Antennas and Propagation*, **vol. AP-46**, no. 1, pp. 133-141, January 1998.

[7]   Sletten, Mark A., "An Ultrawideband, Polarimetric Radar for the Study of Sea Scatter," *IEEE Transactions on Antennas and Propagation*, **vol. AP-42**, no. 11, pp. 1461-1466, November 1994.

[8]   Sadiku, Matthew N.O., *Numerical Techniques in Electromagnetics*, Boca Raton, FL: CRC Press, 1992, pp. 309-311.

[9]   Sturm, J. Michael and James C. West, "Numerical Study of Shadowing in Electromagnetic Scattering from Rough Dielectric Surfaces," *IEEE Transaction on Geoscience and Remote Sensing*, **vol. 36**, no. 5, pp. 1477-1484, September 1998.

[10]   Thorsos, Eric I., "The Validity of the Kirchhoff Approximation for Rough Surface Scattering using a Gaussian Roughness Spectrum," *Journal of the Acoustic Society of America*, **vol. 83**, no. 1, pp. 78-92, January 1988.

[11] Trizna, Dennis B., "Statistics of Low Grazing Angle Radar Sea Scatter for Moderate and Fully Develop Ocean Waves," *IEEE Transactions on Antennas and Propagation*, vol. **AP-39**, no. 12, pp. 1681-1690, December 1991.

[12] West, James C., "Effect of Shadowing on Electromagnetic Scattering from Rough Ocean Wavelike Surfaces at Small Grazing Angles," *IEEE Transactions on Geoscience and Remote Sensing*, vol. **35**, no. 2, pp. 293-310, March 1997.

[13] West, James C., "Electromagnetic Scattering from Finite Conductivity Wind-Roughened Water Surfaces," *International Journal or Remote Sensing*, vol. **20**, no. 17, pp. 3445-3450, 1999.

[14] West, James C., "LGA Sea-Spike Backscattering from Plunging Breaker Crests," *IEEE Transactions on Geoscience and Remote Sensing*, in press.

[15] West, James C., J. Michael Sturm, and Shiou-Jhy Ja, "Low-Grazing Scattering from Breaking Water Waves Using an Impedance Boundary MM/GTD Approach," *IEEE Transactions on Antennas and Propagation*, vol. **AP-46**, no. 1, pp. 93-100, January 1998.

[16] Ja, Shiou-Jyh, James C. West, Haibing Qiao, and James H. Duncan, "Mechanisms of Low-Grazing-Angle Scatting from Spilling Breaker Water Waves", *Radio Science*, vol. **36**, no. 5, pp. 981-998, Sept./Oct. 2001.

[17] West, James C. and Mark A. Sletten, "Mulitpath EM Scattering from Breaking Ocean Waves at Grazing Incidence," *Radio Science*, vol. **32**, no. 4, pp. 1455-1467, July-August 1997.

[18] West, J.C., B.S. O'Leary, and J. Klinke, "Numerical Calculation of Electromagnetic Scattering from Measured Wind-Roughened Water Surfaces," *International Journal of Remote Sensing*, vol. **19**, no. 7, pp. 1377-1393, 1998.

[19] West, James C., "Ray Analysis of Low-Grazing Scattering from a Breaking Water Wave," *IEEE Transactions on Geoscience and Remote Sensing*, vol. **37**, no. 6, pp. 2725-2727, November 1999.

[20] Harrington, Roger F., *Field Computation by Moment Methods*, Malabar, Florida: Robert E. Krieger Publishing Company, 1968, pp 1-19, 41-61.

[21] West, James C. and Zhiquin Zhao, "Electromagnetic Modeling of Multipath Scattering from Breaking Water Waves with Rough Faces," *IEEE Transactions on Geoscience and Remote Sensing*, in press.

[22] Holliday, Dennis, Lester L. DeRaad, Jr., and Gaetan J. St-Cyr, " Sea-Spike Scattering from a Steepening Wave," *IEEE Transactions on Antennas and Propagation*, vol. **46**, no. 1, pp. 108-113, January 1998.

[23] Trizna, Dennis B., "A Model for Brewster Angle Damping and Multipath Effects on the Microwave Radar Sea Echo at Low Grazing Angles," *IEEE Transactions on Geoscience and Remote Sensing*, **vol. 35**, no. 5, pp. 1232-1244, September 1997.

[24] Sletten, Mark A., Dennis B. Trizna, and James P. Hansen, "Ultrawide-Band Radar Observations of Multipath Propagation Over the Sea Surface," *IEEE Transactions on Antennas and Propagation*, **vol. 44**, no. 5, pp. 646-651, May 1996.

[25] Lyzenga, D.R., A.L. Maffett, and R.A. Shuchman, "The Contribution of Wedge Scattering to the Radar Cross Section of the Ocean Surface," *IEEE Transactions on Geoscience and Remote Sensing*, **vol. 21**, no. 4, pp. 502-505, 1983.

[26] Kalmykov, A. I. And V.V. Pustovoytenko, "On Polarization features of Radio Signals Scattered from the Sea Surface at Small Grazing Angles," *Journal of Geophysical Research*, **vol. 81**, no. 12, pp. 1960-1964, 1976.

[27] Kalmykov, A.I., A.S. Kurekin, Y.A. Lementa, I.Y. Ostrovskiy, and V.V. Pustovoytenko, "Scattering of Microwave Radiation by Breaking Sea Waves," *Gor'k. Radiofiz.*, **vol. 19**, pp. 1315-1321, 1976.

[28] Sletten, M.A., Personal communication, November, 2001.

∿

VITA

Brent H. Davis

Candidate for the Degree of

Master of Science

Thesis: NUMERICAL STUDY AND COMPARISON OF ELECTROMAGNETIC SCATTTERING FROM OCEAN SURFACES

Major Field: Electrical Engineering

Biographical:

    Personal Data: Born in Kansas City, Missouri, on July 20, 1977, the son of Joe and Diane Davis.

    Education: Graduated from Fort Smith Christian High School, Fort Smith, Arkansas, in May 1995; received Bachelor of Science degree in Electrical Engineering from Oklahoma State University, Stillwater, Oklahoma, in May 2000. Completed the requirements for the Master of Science degree with a major in Electrical Engineering at Oklahoma State University in December 2001.

    Experience: Employed by Oklahoma State University, Department of Electrical and Computer Engineering as a graduate research assistant; Oklahoma State University, Department of Electrical and Computer Engineering, 2000 to present.